Generation of Low-Frequency Spiciness Variability in the Thermocline*

THOMAS KILPATRICK AND NIKLAS SCHNEIDER

Department of Oceanography, and International Pacific Research Center, University of Hawaii at Manoa, Honolulu, Hawaii

EMANUELE DI LORENZO

School of Earth and Atmospheric Sciences, Georgia Institute of Technology, Atlanta, Georgia

(Manuscript received 8 February 2010, in final form 23 July 2010)

ABSTRACT

The generation of variance by anomalous advection of a passive tracer in the thermocline is investigated using the example of density-compensated temperature and salinity anomalies, or spiciness. A coupled Markov model is developed in which wind stress curl forces the large-scale baroclinic ocean pressure that in turn controls the anomalous geostrophic advection of spiciness. The ''double integration'' of white noise atmospheric forcing by this Markov model results in a frequency (ω) spectrum of large-scale spiciness proportional to ω^{-4}, so that spiciness variability is concentrated at low frequencies.

An eddy-permitting regional model hindcast of the northeast Pacific (1950–2007) confirms that time series of large-scale spiciness variability are exceptionally smooth, with frequency spectra $\propto \omega^{-4}$ for frequencies greater than 0.2 cpy. At shorter spatial scales (wavelengths less than ~500 km), the spiciness frequency spectrum is whitened by mesoscale eddies, but this eddy-forced variability can be filtered out by spatially averaging. Large-scale and long-term measurements are needed to observe the variance of spiciness or any other passive tracer subject to anomalous advection in the thermocline.

1. Introduction

The dynamics of low-frequency temperature anomalies depend on whether a density signature exists (Iselin 1939; Liu and Shin 1999; Schneider 1999). Temperature anomalies with a density signature are governed by planetary wave dynamics, whereas those that are density compensated by salinity anomalies behave as a passive tracer in the upper ocean. Density-compensated salinity and temperature variability is known as spiciness (Veronis 1972; Munk 1981) with hot and salty water having high spiciness.

Advection of spiciness anomalies in the thermocline couples the mid- and low-latitude oceans and may play an important role in climate variations (Gu and Philander 1997; Williams et al. 2007). The northeast and southeast subtropical Pacific are favorable regions for generating surface spiciness variability due to a strong lateral spiciness gradient (Yeager and Large 2004, 2007; Johnson 2006; Nonaka and Sasaki 2007) and prominent interannual and decadal anomalies have been observed in the California Current (Chelton et al. 1982; Roemmich and McGowan 1995; Schwing and Mendelssohn 1997; Bograd and Lynn 2003; Schneider et al. 2005; Di Lorenzo et al. 2008). These midlatitude spiciness anomalies are subducted and propagate in the thermocline (Sasaki et al. 2010; Ren and Riser 2010) past observation points such as the Hawaii Ocean Time series (HOT) that show prominent water mass changes (Lukas 2001; Lukas and Santiago-Mandujano 2008). Part of these anomalies may resurface in the upwelling regions of the equatorial Pacific (Fukumori et al. 2004) and alter air–sea interaction and the tropical climate (Schneider 2004). A feedback loop results if the midlatitude imprint of this atmospheric response affects the generation region, producing low-frequency climate variations (Gu and Philander 1997; Schneider 2000). Aspects of these processes have been described in other ocean basins such as the South Pacific (Yeager and Large 2004, 2007; Luo et al. 2005; Nonaka and Sasaki 2007) and North Atlantic (Laurian et al. 2006, 2009).

---

* International Pacific Research Center Publication Number 726 and School of Ocean and Earth Science Technology Publication Number 8032.

Corresponding author address: Thomas Kilpatrick, Department of Oceanography, University of Hawaii at Manoa, 1000 Pope Road, Honolulu, HI 96822.
E-mail: thomaski@hawaii.edu

DOI: 10.1175/2010JPO4443.1

Even in the absence of a feedback loop, decadal climate variability results from these processes when driven by stochastic atmospheric forcing that has variance at all time scales (James and James 1989). The ocean low pass filters this stochastic forcing (Hasselmann 1976), accounting for the ubiquitous frequency spectra of sea surface temperature, ocean pressure, and surface temperature climate indices such as the Pacific decadal oscillation, which are white for low frequencies and proportional to ω^{-2} for high frequencies, a -2 slope of the spectra in a log–log plot (Frankignoul and Hasselmann 1977; Frankignoul et al. 1997; Davis 1976; Mantua et al. 1997; Schneider and Cornuelle 2005).

Here, it is shown that stochastically forced anomalous advection in the thermocline leads to spiciness variability with frequency spectra cutoff at decadal time scales and a frequency slope of -4, an even sharper concentration of the variance at low frequencies. To this end, section 2 reviews spiciness dynamics and develops a coupled Markov model for anomalous geostrophic advection. These dynamics are explored in multiple realizations of a high-resolution primitive equation model that enables a comparison of the spiciness variability forced by the atmosphere and that due to oceanic nonlinear internal mechanisms. The model and integrations are introduced in section 3. Section 4 identifies the wind-forced spiciness signal, which is shown in section 5 to result from the Ekman pumping-forced geostrophic flow. Section 6 discusses the detection of atmospherically forced spiciness signals in a strong ocean eddy field. The dual contributions of anomalous advection and surface freshwater flux variability to interior spiciness are compared in section 7, and section 8 provides a summary and discussion.

2. Theory for anomalous geostrophic advection

This section reviews spiciness dynamics and develops a coupled Markov model to explain the spiciness frequency spectra resulting from stochastically forced anomalous geostrophic advection.

Conservation of salinity can be written using potential density (σ_θ) as the vertical coordinate,

$$\frac{\partial S}{\partial t} + \mathbf{u}_h \cdot \nabla_h S + \dot{\sigma}_\theta \frac{\partial S}{\partial \sigma_\theta} = 0, \qquad (1)$$

where subgridscale fluxes are neglected, ∇_h is taken along constant σ_θ isopycnal surfaces, and $\dot{\sigma}_\theta = D\sigma_\theta/Dt$ [Eq. (3.157) in Vallis 2006]. The vertical velocity can be neglected because of the small diapycnal mixing rates in the interior ocean (Ledwell et al. 1993), resulting in an equation for salinity on an isopycnal surface, or spiciness.

The S and $\mathbf{u}_h$ fields are decomposed into the seasonal climatology (denoted with an overbar) and anomalies (denoted with a prime) by averaging along constant σ_θ isopycnal surfaces. Subtracting seasonal means results in an equation for the isopycnal salinity anomaly,

$$\left(\frac{\partial}{\partial t} + \overline{\mathbf{u}}_h \cdot \nabla_h\right) S' = -\mathbf{u}'_h \cdot \nabla_h \overline{S} - \Gamma, \qquad (2)$$

with the influence of the covarying $\mathbf{u}'_h$ and S' fields given by

$$\Gamma = \mathbf{u}'_h \cdot \nabla_h S' - \overline{\mathbf{u}'_h \cdot \nabla_h S'}. \qquad (3)$$

Compressibility of seawater impacts the thermal and haline expansion coefficients and thus acts as a source term on the rhs of Eq. (2), amplifying or attenuating spiciness anomalies as pressure changes along an advection path (Tailleux et al. 2005). The linear eigenmode analysis of Müller and Willebrand (1986) indicates that this effect has a characteristic depth scale of 15 km and time scale of 1000 yr and, therefore, may be important for the adjustment of the deep thermohaline circulation but can be neglected for the depth scale of the upper thermocline (~300 m) of interest in this study.

The first term on the rhs of Eq. (2) describes the forcing of isopycnal salinity variability by anomalous advection; the second term describes the influence of the covarying $\mathbf{u}'_h$ and S' fields. In an eddying ocean, Γ acts both to force and dissipate spiciness anomalies,

$$\Gamma = \Gamma_{\text{for}} + \Gamma_{\text{dis}}. \qquad (4)$$

The mean advection term on the lhs of Eq. (2), although not a physical damping mechanism, acts to limit the stochastically forced spiciness variance (Spall 1993; Frankignoul et al. 1997) and is combined here with Γ_{dis} into a single net ''feedback'' factor μ (Frankignoul and Reynolds 1983) such that Eq. (2) becomes

$$\frac{\partial S'}{\partial t} = -\mu S' - \mathbf{u}'_h \cdot \nabla_h \overline{S} - \Gamma_{\text{for}}, \qquad (5)$$

where μ^{-1} gives the time scale of the feedback on S', estimated here from the primitive equation model experiments described in section 3 and considered spatially uniform, a simplification to be discussed. The spiciness variance due to Γ_{for} is large because of small-scale eddies but will be filtered out of the primitive equation experiments by this study's focus on $O(1000\text{ km})$ scales (see section 6). This leaves the anomalous advection mechanism as the remaining large-scale subsurface forcing, or

$$\frac{\partial S'}{\partial t} = -\mu S' - \mathbf{u}'_h \cdot \nabla_h \overline{S}. \qquad (6)$$

The first baroclinic mode dominates the large-scale, geostrophic motions in the thermocline described by $\mathbf{u}'_h$ in Eq. (6), so a 1½-layer reduced-gravity model captures the important dynamics. For the large-scale response to wind stress, the long-wavelength approximation is justified and the first baroclinic mode pressure is governed by the linear vorticity equation (Qiu 2003)

$$\frac{\partial \eta'}{\partial t} - c_R \frac{\partial \eta'}{\partial x} = -\frac{g' \mathbf{e}_z \cdot \nabla \times \boldsymbol{\tau}'}{\rho_0 g f}, \tag{7}$$

where η is sea surface height (SSH), c_R is the phase speed of long first baroclinic mode Rossby waves, g' is the reduced gravity, ρ_0 is the reference density, $\mathbf{e}_z$ is the unit vector in the vertical direction, $\boldsymbol{\tau}$ is the horizontal wind stress vector, and f is the Coriolis parameter. The subscript is dropped from the gradient operator for the 1½-layer model.

The decorrelation time scale for the atmosphere T_{atm} is on the order of a few days, so for $\omega \ll T_{\text{atm}}^{-1}$ the wind stress curl is unpredictable and can be represented as white noise stochastic forcing (Hasselmann 1976; Frankignoul and Hasselmann 1977; Lagerloef 1995; Frankignoul et al. 1997; Cummins and Lagerloef 2002, 2004). A Markov model for the first baroclinic mode pressure based on Eq. (7) is

$$\frac{\partial \eta'}{\partial t} = -\lambda \eta' + \gamma C', \tag{8}$$

where γ is a scaling coefficient, C is the stochastic wind stress curl, and λ is the linear feedback on pressure anomalies, representing higher-order physics neglected in Eq. (7). The Rossby wave term in Eq. (7) is omitted because large-scale interannual variability of the first baroclinic mode pressure in the northeast Pacific is dominated by the local response to wind stress curl (Cummins and Lagerloef 2004).

The wind stress curl frequency spectrum $F_{\text{CC}}(\omega)$ is white for $\omega \ll T_{\text{atm}}^{-1}$ and denoted $F_{\text{CC}}(0)$ (Hasselmann 1976). The frequency spectrum of the first baroclinic mode pressure follows from Eq. (8) and for $\omega \ll T_{\text{atm}}^{-1}$ is given by

$$F_{\eta\eta}(\omega) = \frac{\gamma^2 F_{\text{CC}}(0)}{\omega^2 + \lambda^2}. \tag{9}$$

The frequency spectrum is proportional to ω^{-2} for $\lambda < \omega \ll T_{\text{atm}}^{-1}$ and white for $\omega < \lambda$, with λ determined by the internal feedback mechanism (Frankignoul and Hasselmann 1977).

In the long-wavelength, low-frequency approximation, horizontal currents are geostrophically balanced, and

$$\mathbf{u}'_h = \frac{g}{f} \mathbf{e}_z \times \nabla \eta'$$

is substituted into Eq. (6) to explicitly show the forcing of isopycnal salinity by the first baroclinic mode pressure,

$$\frac{\partial S'}{\partial t} = -\mu S' + \frac{g}{f} \mathbf{e}_z \cdot (\nabla \overline{S} \times \nabla \eta'). \tag{10}$$

With the approximation that $\nabla \overline{S}$ always points in the same direction, a new coordinate r is defined such that the unit vector

$$\mathbf{e}_r = \mathbf{e}_z \times \frac{\nabla \overline{S}}{|\nabla \overline{S}|}.$$

Defining the scaling coefficient $\varepsilon = f^{-1} g |\nabla \overline{S}|$, Eq. (10) is written as

$$\frac{\partial S'}{\partial t} = -\mu S' + \varepsilon \frac{\partial \eta'}{\partial r}. \tag{11}$$

Fourier transforms in space (denoted with a caret) of Eqs. (8) and (11) yield a coupled Markov model for spiciness variability generated by anomalous geostrophic advection,

$$\frac{\partial \hat{\eta}}{\partial t} = -\lambda \hat{\eta} + \gamma \hat{C} \tag{12}$$

$$\frac{\partial \hat{S}}{\partial t} = -\mu \hat{S} + \varepsilon i k \hat{\eta}, \tag{13}$$

for wavenumber k in the r direction. Stochastic Ekman pumping forces the first baroclinic mode pressure, which in turn forces spiciness. One only expects Eq. (13) to be valid for k corresponding to long-wavelength spiciness variability, where the Ekman pumping dynamics of Eq. (12) dominate.

The wavenumber–frequency spectrum of the first baroclinic mode pressure derived from Eq. (12) is

$$F_{\eta\eta}(k, \omega) = \frac{\gamma^2 F_{\text{CC}}(k, 0)}{\omega^2 + \lambda^2}, \tag{14}$$

again for k corresponding to long wavelengths and $\omega \ll T_{\text{atm}}^{-1}$. The wavenumber–frequency spectrum of spiciness for $\omega \ll T_{\text{atm}}^{-1}$ follows from Eqs. (13) and (14),

$$F_{\text{SS}}(k, \omega) = \frac{(\varepsilon k)^2 F_{\eta\eta}(k, \omega)}{\omega^2 + \mu^2} \tag{15}$$

$$= \frac{(\varepsilon k \gamma)^2 F_{\text{CC}}(k, 0)}{\omega^4 + (\mu^2 + \lambda^2)\omega^2 + \mu^2 \lambda^2}. \tag{16}$$

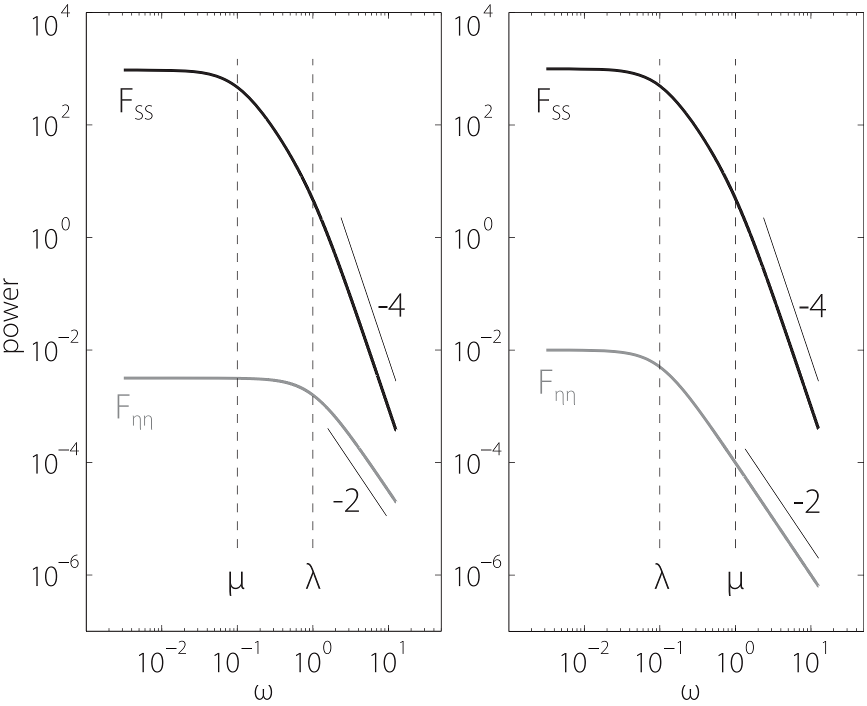

FIG. 1. Frequency spectra predicted by the anomalous geostrophic advection model [Eqs. (14) and (16)] for a single k corresponding to long-wavelength spiciness S and first baroclinic mode pressure η: (left) for the case $\mu < \lambda$ and (right) for $\mu > \lambda$. The axes are dimensionless; only spectral slopes are considered. Note that ω is the angular frequency.

The ''double integration'' of atmospheric forcing results in $F_{SS} \propto \omega^{-4}$ for long wavelengths (Fig. 1), an even sharper concentration of variance at low frequencies than for pressure. If μ and λ have similar magnitude, the long-wavelength spiciness spectrum transitions smoothly from a 0 slope for $\omega < \min(\mu, \lambda)$ to a -4 slope for $\omega > \max(\mu, \lambda)$. If μ and λ differ greatly, an intermediate -2 slope region exists for $\min(\mu, \lambda) < \omega < \max(\mu, \lambda)$.

Equations (12) and (13) represent the simplest possible model that can explain the $F_{SS} \propto \omega^{-4}$ dependence of spiciness variability generated by stochastically forced anomalous geostrophic advection. This model only applies to long-wavelength variability generated in the thermocline: that is, away from the surface where $\mathbf{u}'_h$ includes higher-frequency Ekman currents. The orientation of $\nabla\overline{S}$ has been considered constant and the effects of mean advection and Rossby waves on the variation of F_{SS} in space have been neglected.

3. Primitive equation model

To test whether the frequency spectra of long-wavelength spiciness show the predicted -4 slope requires very long time series of temperature and salinity. Lacking such observational datasets, numerical simulations are performed with the Regional Ocean Modeling System (ROMS).

a. ROMS configuration

ROMS is a free-surface primitive equation model described in detail in Marchesiello et al. (2003) and Shchepetkin and McWilliams (2005). The model realizations R20a, R20b, and R10 are summarized in Table 1. Two grids were used with the same domain and vertical resolution consisting of 30 levels, but different horizontal resolution. The domain extends zonally from 180° to 112°W and meridionally from 25° to 61°N. Zonal resolution is 0.25° for realizations R20a and R20b and 0.125° for R10. The spatial resolution increases toward the north to better resolve the deformation radius.

Boundary conditions and forcing are the same for all three realizations, but initial conditions differ. The 0.25° grid realizations R20a and R20b, each 55 years, were performed in succession after a 53-yr spinup. The wind forcing was reset from 2004 to 1950 between realizations, so the initial condition for R20a is the final state of the spinup and the initial condition for R20b is the final state of R20a, corresponding to December 2004. Likewise, the initial condition for R10 is the final state of a spinup run on the 0.125° grid.

Open boundary conditions (Marchesiello et al. 2001) are used at the western and southern lateral boundaries, where the model is nudged toward monthly mean

TABLE 1. Realizations of northeast Pacific ROMS simulations. The boundary conditions and forcing are the same for each realization, but initial conditions differ.

Realization	Zonal resolution	Spatial resolution	Grid points ($Y \times X \times Z$)	Integration period
R20a	0.25°	14–24 km	$210 \times 274 \times 30$	1950–2004
R20b	0.25°	14–24 km	$210 \times 274 \times 30$	1950–2004
R10	0.125°	7–12 km	$418 \times 546 \times 30$	1950–2007

climatological values (Levitus et al. 1994). A radiation boundary condition is used, with a nudging time scale of 1 day for flow into the model domain and a time scale of 1 yr for flow out of the domain.

The wind stress is from the National Centers for Environmental Prediction–National Center for Atmospheric Research (NCEP–NCAR) reanalysis for 1950–2007 (Kalnay et al. 1996). The *K*-profile parameterization (KPP) vertical mixing scheme (Large et al. 1994) is used in the surface boundary layer; however, the use of 1-month-averaged wind stress results in model mixed layers that are unrealistically shallow (de Boyer Montégut et al. 2004).

NCEP–NCAR surface heat fluxes are also used, with a relaxation to the time-dependent monthly mean SST from the National Oceanic and Atmospheric Administration (Smith and Reynolds 2004). The nudging time scale is 1 month.

In contrast to GCMs such as the OGCM for the Earth Simulator (Masumoto et al. 2004), surface salinity is only forced by a prescribed surface freshwater flux. The freshwater flux contains a seasonal cycle but no interannual variability, so interannual salinity variability is due only to changes in the flow field and mixing. The freshwater flux was determined from a prior ‘‘climatological’’ run (not shown in table) that relaxed surface salinity to observed values; the corrections were stored and converted to a climatological freshwater flux for use here. Note that the use of a regional model limits the salinity errors that can grow large in long GCM integrations due to errors in boundary conditions, mixing, or flow fields.

All ROMS output was saved as monthly means. To isolate the nonseasonal variability, a linear trend of about 9×10^{-4} psu yr^{-1} and the mean seasonal cycle were removed.

b. Model validation

Realizations R20a and R20b give realistic results and have been used successfully in previous studies of the northeast Pacific: Di Lorenzo et al. (2008) showed that the model surface salinity near California compared well with observations from California Cooperative Oceanic Fisheries Investigations and Scripps Pier and tracked the North Pacific Gyre Oscillation (NPGO) index of SSH variability; Di Lorenzo et al. (2009) showed that model salinity at line P in the Gulf of Alaska also matched observations and tracked the NPGO; Chhak et al. (2009) showed that the first and second EOF patterns and principal components of model SSH matched the altimeter record for 1993–2004; and Combes and Di Lorenzo (2007) compared model SSH at individual grid points to tide gauges in the Gulf of Alaska and found that the model skill was comparable to satellite observations.

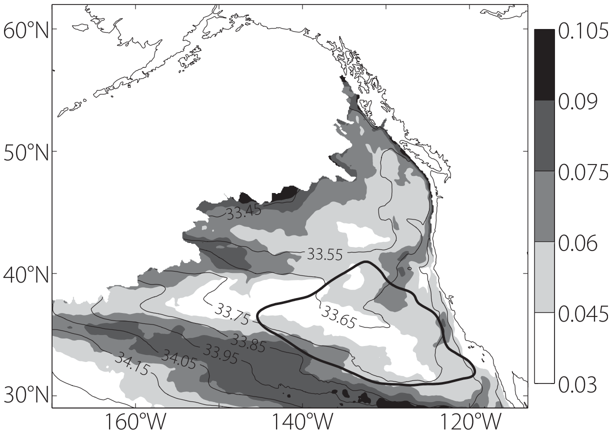

FIG. 2. Salinity (psu) standard deviation (shade) and mean (thin contours) on the $\sigma_\theta = 26$ kg m^{-3} isopycnal surface. The thick contour outlines the mask for the S_{10} signal. The white space in the northwest part of the domain indicates grid points that outcropped for at least one month.

The R10 mean salinity distribution on the $\sigma_\theta = 26$ kg m^{-3} isopycnal surface shows the fresh tongue of the California Current extending southward, collocated with a local minimum in variance (Fig. 2). Strong gradients in mean salinity to the southwest are collocated with the highest variance. The white area in the northwest part of the domain indicates where the isopycnal outcropped for at least one month. The salinity variance and mean distributions on the same isopycnal for R20a and R20b (not shown) look similar to Fig. 2.

Henceforth only nonseasonal variability is considered in isopycnal salinity, SSH, and wind stress curl, so the prime notation is dropped: S, η, and C represent anomalies. Note that S, η, and C are spatially averaged where indicated but the full monthly time resolution is retained for all analyses.

4. Identifying the wind-forced signal

The model solutions diverge because of their different initial conditions and the chaotic nature of the ocean circulation. Thus, the shared spiciness variance between

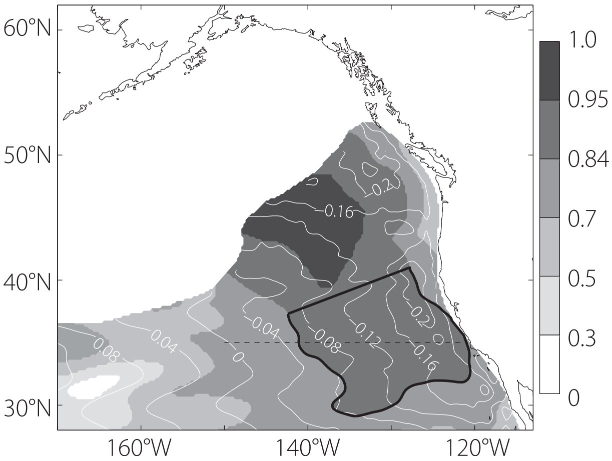

FIG. 3. The $\sigma_\theta = 26$ kg m^{-3} isopycnal salinity correlation between realizations R20a and R20b (shading; note nonlinear grayscale). The isopycnal salinity was first spatially averaged over 550 km × 550 km squares but not time averaged. The mask indicated by the thick black line, following the 0.84 contour, is used to define S_{20a} and S_{20b}. The dashed line at 35°N is the location of the vertical sections in Fig. 6. White space in the northwest part of the domain represents grid points that outcropped for at least one month. White contours show mean M/g (m), for the Montgomery potential, $M = g\eta + g\rho_0^{-1}\int_z^0 dz'\delta\rho + g\rho_0^{-1}z\delta\rho$, with the perturbation density given by $\delta\rho = \rho - \rho_0$ (Vallis 2006), and indicate equatorward flow through the southern half of the isopycnal. Note that the use of M here is consistent with section 2 because M on the $\sigma_\theta = 26$ kg m^{-3} isopycnal is dominated by the first baroclinic mode and has similar spectral characteristics.

R20a and R20b is attributed to the (identical) wind forcing and the remainder to oceanic nonlinear internal variability. In this section, the spiciness changes due to oceanic internal variability are filtered out to focus on the wind-forced signal. Large-scale wind-forced variability corresponds to the anomalous advection term on the rhs of Eq. (5) and oceanic internal variability to the eddy term, as previous analyses of the same ROMS experiments used here (Di Lorenzo et al. 2008; Chhak et al. 2009) have shown that large-scale winds dominate the low-frequency variability in the northeast Pacific and that chaotic large-scale, eddy-forced accelerations of the California Current System, hypothesized by Schneider et al. (2005), are not important for decadal variability.

The spiciness field on the $\sigma_\theta = 26$ kg m^{-3} isopycnal (Fig. 2) includes high-variance, short-wavelength, eddy-forced anomalies (see section 6), so a 550 km × 550 km spatial average is applied to help isolate the large-scale wind-forced signal. High point-to-point correlations between the R20a and R20b spatially averaged isopycnal salinity fields indicate that wind-forced variability dominates in a "tongue" extending southeastward from the outcrop region (Fig. 3), whereas lower correlations to the southwest are evidence of oceanic internal variability.

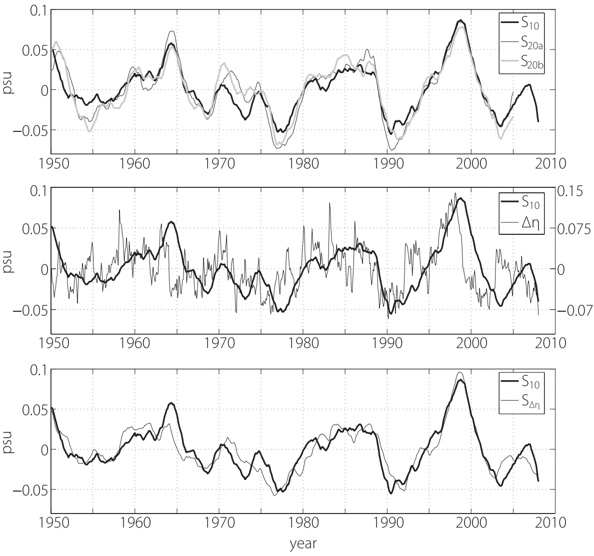

FIG. 4. Isopycnal salinity and SSH anomaly indices. Anomalies have been spatially averaged, but no time averaging has been applied. See Table 2 for descriptions of the indices. (top) Isopycnal salinity indices S_{10}, S_{20a}, and S_{20b} (psu). The correlation between S_{20a} and S_{20b} is 0.95; between S_{10} and S_{20a} is 0.93; and between S_{10} and S_{20b} is 0.91. (middle) S_{10} and $\Delta\eta$ (m); high values of $\Delta\eta$ indicate weaker equatorward geostrophic transport. Note that the salinity scale is on the left and the SSH scale is on the right. (bottom) S_{10} and $S_{\Delta\eta}$, which have a correlation of 0.89.

The northern part of the tongue is shallow and close to the outcrop, whereas the southern part is deep and removed from the surface mixed layer. It is shown below that the correlation of the spiciness signal in the southern half of the tongue among realizations is larger than the correlation to the upstream condition (outcrop) in individual realizations, indicating that the signal is generated locally. Thus, the southern half of the tongue is the optimal location for testing the anomalous advection dynamics of section 2.

A spiciness mask is formed along the 0.84 contour in the southern half of the tongue (Fig. 3, thick black line). The isopycnal salinity anomalies averaged spatially over the mask for realizations R20a and R20b are defined as S_{20a} and S_{20b}, respectively (Fig. 4, top). All isopycnal salinity signals in this paper are summarized in Table 2. The S_{20a} and S_{20b} indices are nearly identical, with a correlation of 0.95, and very smooth. A very similar signal is found in R10 with a slightly adjusted mask shape (Fig. 2), chosen by maximizing the correlation with S_{20a} and S_{20b}. The isopycnal salinity spatially averaged over this mask is defined as S_{10} and has correlations to S_{20a} and S_{20b} of 0.93 and 0.91, respectively (Fig. 4, top). The S_{10} signal is the focus of this study.

As mentioned above, the spiciness mask is selected as a region where the local wind-forced generation is

TABLE 2. Summary of isopycnal salinity (S), SSH (η), and wind stress curl (C) indices.

Index	Realization	Defined by	Mask
S_{20a}	R20a	Area avg	Fig. 3, thick line
S_{20b}	R20b	Area avg	Fig. 3, thick line
S_{10}	R10	Area avg	Fig. 2, thick line
$S_{\Delta\eta}$	R10	Eq. (21)	—
S_{curl}	R10	Eq. (23)	—
η_{10}	R10	Area avg	Fig. 7, offshore mask
η_{coast}	R10	Area avg	Fig. 7, coastal mask
$\Delta\eta$	R10	$= \eta_{\mathrm{coast}} - \eta_{10}$	—
η_{curl}	R10	Eq. (22)	—
C_{10}	R10	Area avg	Fig. 7, offshore mask

stronger than the influence of subducting outcrop anomalies. The correlation between realizations exceeds 0.84 in the mask (Fig. 3), higher than the S_{10} correlations to the prior outcrop signal at lags of 9, 18, and 27 months (Fig. 5), indicating that S_{10} is generated locally and justifies the neglect of mean advection in the section 2 Markov model [Eqs. (12) and (13)].

The S_{10} signal is concentrated in the thermocline, with a weak expression at the surface. At 35°N, the maximum salinity correlations to S_{10} occur at 150–220-m depth, near the mean depth of the $\sigma_\theta = 26$ kg m^{-3} isopycnal (Fig. 6, top). The maximum expression of S_{10} is thus deeper and farther west than the strongest equatorward flow (Fig. 6, bottom), indicating that S_{10} is associated more with the ventilated thermocline than the California Current.

5. Wind forcing

A smooth, wind-forced, long-wavelength spiciness signal exists in the model thermocline. In this section, it is shown that the signal is generated by local, wind-forced anomalous geostrophic advection.

a. Forcing by anomalous geostrophic advection

To test the anomalous geostrophic advection model [Eq. (11)] for the S_{10} signal, one must first determine where to measure the pressure gradient. As explained in section 2, SSH is used in place of the first baroclinic mode pressure. The sensitivity of S_{10} to the pressure field is then determined as follows: S_{10} and the SSH anomaly time series at each grid point are fit to a discretized anomalous advection model sans spatial derivative,

$$\frac{S_{10}^{j+1} - S_{10}^{j}}{\Delta t} = -\mu S_{10}^{j} + \epsilon(x,y)\eta^{j}(x,y). \qquad (17)$$

The coefficient $\epsilon(x, y)$, replacing ε in Eq. (11), is determined by least squares, with $\Delta t = 1$ month, the time index $j = \{1, 2, \ldots, 695\}$, and the damping term $\mu = 0.5$ yr^{-1} estimated

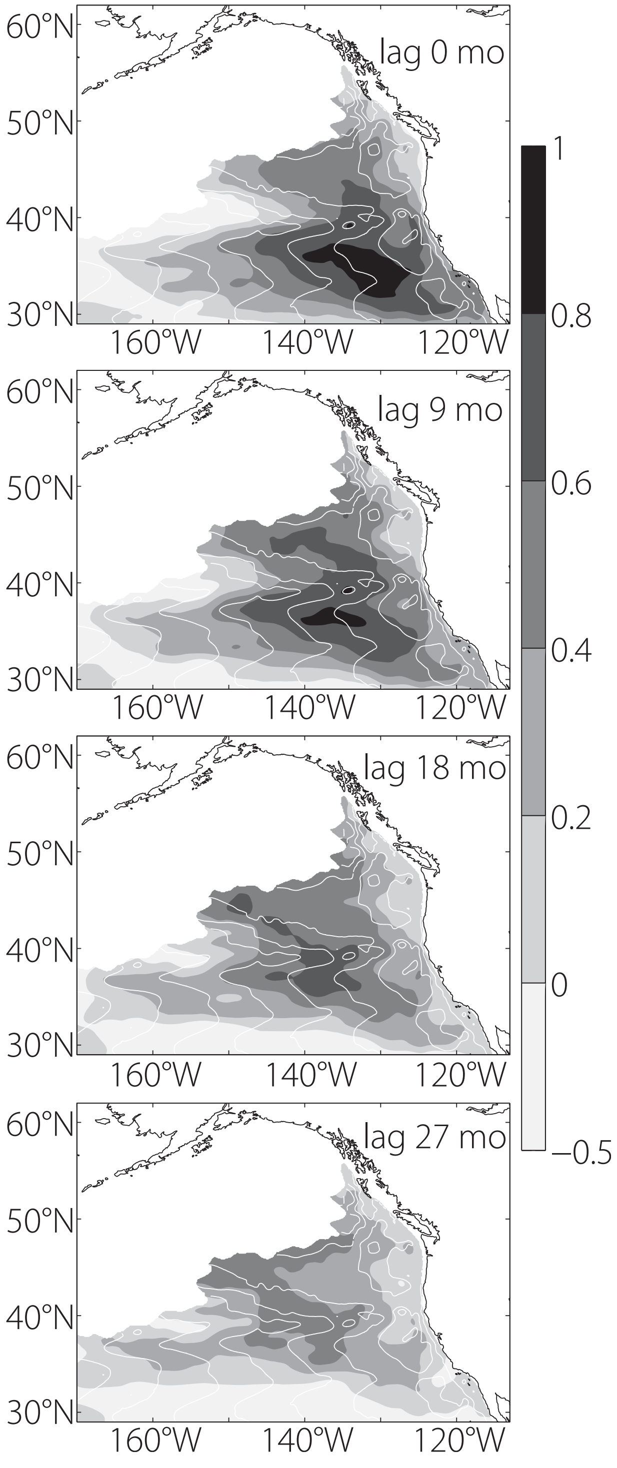

FIG. 5. Correlation of S_{10} to the prior $\sigma_\theta = 26$ kg m^{-3} isopycnal salinity at lags of 0, 9, 18, and 27 months (shading; note nonlinear grayscale). The isopycnal salinity was spatially averaged over 550 km × 550 km squares prior to computing the correlation. White contours show mean M/g (CI = 0.04 m) for realization R10, where M is the Montgomery potential.

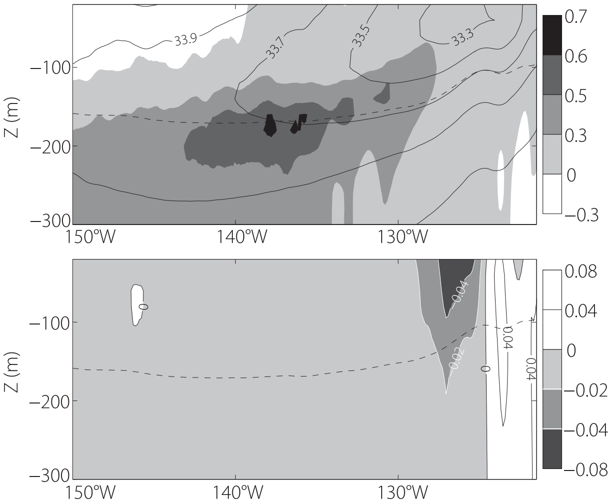

FIG. 6. Vertical sections at 35°N (cf. dashed line in Fig. 3): (top) salinity correlation to S_{10} computed along constant z surfaces (shade) and mean salinity (contours; psu) and (bottom) mean meridional velocity (m s^{-1}). Note the nonlinear grayscales. In both plots, the dashed line is the mean depth of the $\sigma_\theta = 26$ kg m^{-3} isopycnal. The salinity minimum corresponds to the strongest equatorward velocity located in the core of the California Current, but S_{10} has its strongest expression in the weaker and deeper flow to the west.

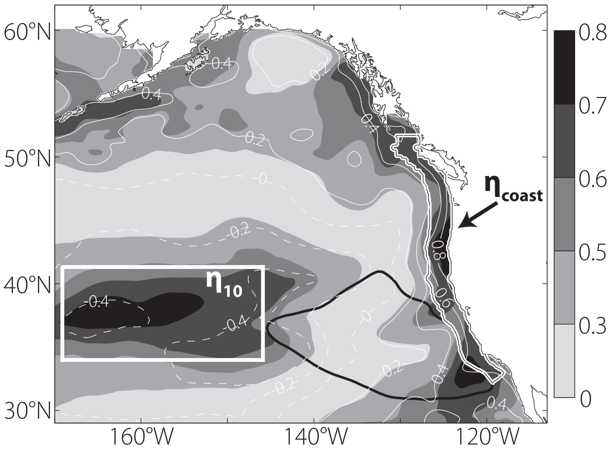

FIG. 7. Skill of the Markov model for SSH forcing S_{10} [Eq. (17)], measured at each grid point by the correlation between S_{10} and the reconstructed spiciness (shade). The SSH was spatially averaged over 350 km × 350 km squares prior to testing the Markov model. Thin white contours indicate the value of ϵ (psu yr^{-1} m^{-1}), determined from a least squares fit of the data to Eq. (17) with fixed $\mu = 0.5$ yr^{-1}. Note that $\epsilon \le 0$ and $\epsilon > 0$ are indicated by dashed and solid contours, respectively. The thick white line outlines the SSH mask used to create η_{10}, the thick white line with black trace outlines the mask for η_{coast} (Table 2), and the thick black line outlines the S_{10} mask.

from the S_{10} frequency spectrum (Fig. 8). Results of this section are not sensitive to varying μ in the 0.4–0.6 yr^{-1} range. The S_{10} signal is reconstructed separately at each grid point by integrating from the S_{10} initial value,

$$S^{j+1}(x,y) = S^{j}(x,y)(1-\mu\Delta t) + \epsilon(x,y)\eta^{j}(x,y)\Delta t. \quad (18)$$

The correlations of the reconstructions to S_{10} (Fig. 7, shade) indicate that S_{10} is sensitive to pressure variations along the California coast and offshore, two distinct regions straddling the spiciness mask.

The coefficient $\epsilon(x, y)$ is positive along the coast and negative offshore (Fig. 7, white contours), suggesting that high pressure along the coast and low pressure offshore lead to salty anomalies. This phasing is consistent with anomalous geostrophic advection in the northeast Pacific, as in Eq. (11), where reduced southward transport of freshwater results in salty anomalies.

Indices for the first baroclinic mode coastal pressure η_{coast} and offshore pressure η_{10} are created by spatially averaging SSH over the regions where the Eq. (18) reconstructions have skill (Fig. 7, thick white lines). All pressure indices are summarized in Table 2. The pressure gradient forcing of S_{10} is restored by discretizing $\partial\eta/\partial r$ in Eq. (11),

$$\frac{\partial S_{10}}{\partial t} = -\mu S_{10} + \varepsilon\frac{\Delta\eta}{\Delta r}, \quad (19)$$

with an index for the large-scale pressure gradient given by

$$\Delta\eta = \eta_{\mathrm{coast}} - \eta_{10}. \quad (20)$$

The S_{10} signal lags $\Delta\eta$ (Fig. 4, middle), consistent with Eq. (19), and S_{10} is also much smoother than $\Delta\eta$ with nearly all variance at frequencies below 0.2 cpy. This smoothness is evident in the frequency spectrum of S_{10} (Fig. 8), which shows a −4 slope for frequencies greater than 0.2 cpy, consistent with the anomalous advection model of section 2.

The anomalous geostrophic advection model is tested by integrating Eq. (19) to form $S_{\Delta\eta}$,

$$S_{\Delta\eta}^{j+1} = S_{\Delta\eta}^{j}(1-\mu\Delta t) + \frac{\varepsilon}{\Delta r}\Delta\eta^{j}\Delta t, \quad (21)$$

with $\mu = 0.5$ yr^{-1}, and the coefficient $\varepsilon/\Delta r = 0.65$ psu yr^{-1} m^{-1} selected so that $S_{\Delta\eta}$ has the same sign and variance as S_{10}. Though deviations occur during 1963–65, 1971–73, 1974–76, and 2003–04 (Fig. 4, bottom), possibly due to nonlocal perturbations that reach the interior through mean advection, S_{10} and $S_{\Delta\eta}$ have an outstanding correspondence overall and a correlation of 0.89. The frequency spectrum of $S_{\Delta\eta}$ also shows a −4 slope (Fig. 8). Thus, the anomalous advection model reproduces the phase and frequency spectrum of the spiciness signal.

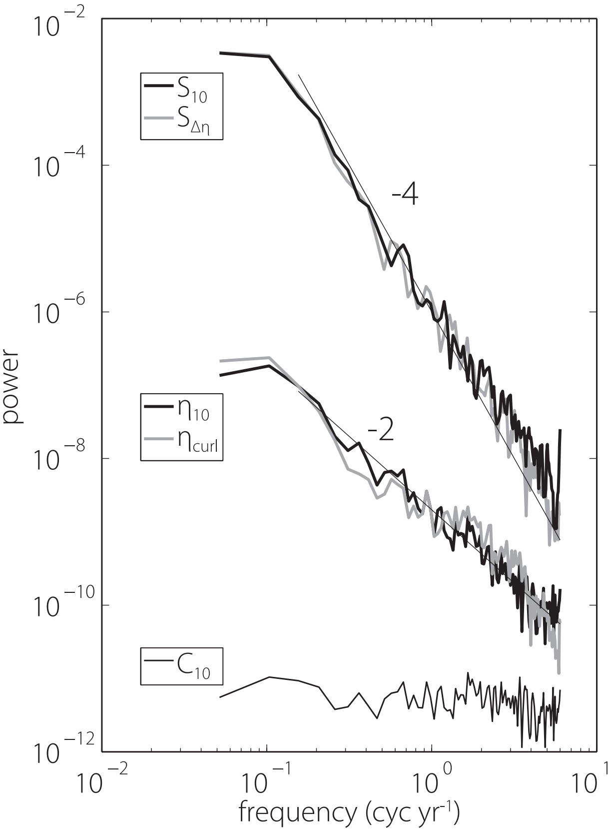

FIG. 8. Frequency spectra of isopycnal salinity, SSH, and wind stress curl indices. See Table 2 for a description of the indices. The *y* axis has no units; only spectral slopes are compared. The thin black lines show −4 and −2 slopes for reference.

The next step is to connect $\Delta\eta$ to the wind stress. In principle, this requires two Markov models of the form of Eq. (8) since $\Delta\eta$ is comprised of two pressure indices. However, η_{10} and $\eta_{\rm coast}$ covary at low frequencies, as their 24-month running means have a −0.65 correlation. Since integrating Eq. (19) with η_{10} as the sole forcing results in a correlation to S_{10} of 0.85, while using $\eta_{\rm coast}$ alone lowers the correlation to 0.76, one can say the offshore pressure variability is more important in forcing S_{10}. For these reasons the next section focuses solely on the Ekman pumping–forced offshore pressure, equivalent to setting $\Delta\eta = -\eta_{10}$ in Eq. (20).

b. Forcing by Ekman pumping

As described in the previous section, the forcing of first baroclinic mode pressure variability by Ekman pumping is only considered in the offshore region (Fig. 7). The offshore pressure index (η_{10}) is reconstructed by integrating Eq. (8) to form $\eta_{\rm curl}$,

$$\eta_{\rm curl}^{j+1} = \eta_{\rm curl}^{j}(1 - \lambda\Delta t) + \gamma C_{10}^{j}\Delta t, \tag{22}$$

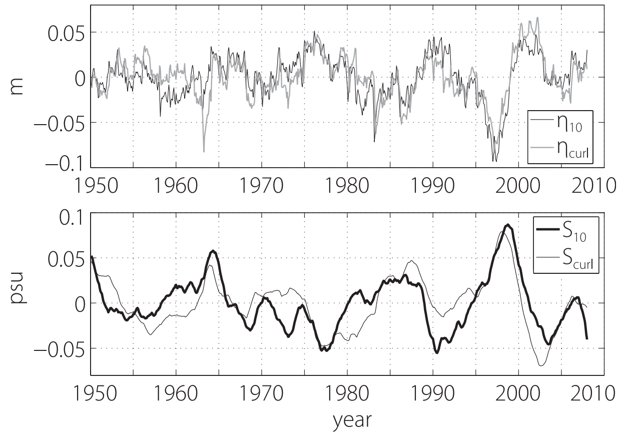

FIG. 9. Time series of (top) η_{10} and $\eta_{\rm curl}$ (m), correlation is 0.72, and (bottom) S_{10} and $S_{\rm curl}$ (psu), correlation is 0.70. See Table 2 for descriptions of the isopycnal salinity and SSH indices.

where C_{10} is the spatially averaged offshore wind stress curl (Table 2). The damping coefficient $\lambda = 0.6\ {\rm yr}^{-1}$ was estimated from the η_{10} frequency spectrum, as the location of the peak when plotted in variance-conserving form (Frankignoul et al. 1997). The scaling coefficient $\gamma = -1.15 \times 10^{-9}\ {\rm kg}^{-1}\ {\rm m}^3\ {\rm yr}$ is selected so that $\eta_{\rm curl}$ has the same sign and variance as η_{10}. The correlation between η_{10} and $\eta_{\rm curl}$ is 0.72 (Fig. 9, top) and the signals have similar frequency spectra (Fig. 8). This local Ekman pumping model captures the variability in η_{10}, consistent with the results of Cummins and Lagerloef (2004) for a larger domain in the northeast Pacific.

The reconstructed pressure, $\eta_{\rm curl}$, is then used to force Eq. (19). The resulting salinity reconstruction $S_{\rm curl}$ is essentially a double integration of the wind stress curl,

$$S_{\rm curl}^{j+1} = S_{\rm curl}^{j}(1 - \mu\Delta t) + \frac{\varepsilon}{\Delta r}(-\eta_{\rm curl}^{j})\Delta t, \tag{23}$$

where the contribution of the coastal pressure to $\Delta\eta$ [Eq. (20)] is neglected. The correlation of $S_{\rm curl}$ and S_{10} is 0.70 (Fig. 9, bottom) for $\mu = 0.5\ {\rm yr}^{-1}$ and $\varepsilon/\Delta r = 1.0\ {\rm psu\ yr}^{-1}\ {\rm m}^{-1}$. Note that $\varepsilon/\Delta r$ is more than double the magnitude of ϵ determined from Eq. (17) (Fig. 7) because least squares fitting seriously underestimates ϵ, as noted before by Lagerloef (1995). Here $S_{\rm curl}$ captures the freshening trend from 1950 to 1955, the salty period from 1963 to 1966, the freshening from 1975 to 1979, the salty period from 1983 to 1989, and the large salinification and subsequent freshening from 1995 to 2005. However, the deviations are wider than for $S_{\Delta\eta}$, particularly for 1957–62, 1972–74, 1980–82, and 1990–95 (cf. Fig. 4, bottom). Nevertheless, the ability of $S_{\rm curl}$ to capture half of the variance of S_{10} illustrates how the ocean generates spiciness variability in the thermocline through the double integration of atmospheric forcing.

The frequency spectrum of C_{10} has nearly a 0 slope, whereas η_{10} and η_{curl} are near -2 and S_{10} is near -4 (Fig. 8). In this picture,

$$\begin{matrix} \nabla \times \boldsymbol{\tau} & \rightarrow & \eta & \rightarrow & S, \\ 0 & & -2 & & -4 \end{matrix} \tag{24}$$

the wind stress curl forces the long-wavelength first baroclinic mode pressure, and pressure forces spiciness. Each successive integration in this forced linear system changes the spectral slope by -2, such that long-wavelength spiciness has virtually none of the high-frequency variance input by the atmosphere.

6. Short-wavelength spiciness variability

The anomalous advection model of section 2 explains the phase and -4 slope frequency spectrum of the long-wavelength spiciness variability. However, for shorter wavelengths, mesoscale eddies become important and Γ_{for} cannot be neglected in Eq. (5). This is evident when computing the frequency spectrum of isopycnal salinity separately at each grid point in the S_{10} mask and then averaging the spectra together. The resulting frequency spectrum integrates over all wavenumbers and is closer to a -2 slope than -4 (Fig. 10), whereas the spatial average used to form S_{10} filters out the high-wavenumber variance, resulting in a -4 slope. The long-wavelength, wind-forced, -4 slope signal is hidden in a short-wavelength, high-variance, eddy-driven signal.

A transition from the long-wavelength to the small-wavelength spiciness regime is seen by Fourier transforming the $\sigma_\theta = 26$ kg m^{-3} isopycnal salinity field into wavenumber–frequency space and computing the power for varying horizontal wavenumber $|\mathbf{k}|$. At the lowest resolved $|\mathbf{k}|$, corresponding to a wavelength of 1330 km, a -4 slope is clearly seen in the frequency spectrum (Fig. 11). At higher wavenumbers, both diminishing power and a flatter spectral slope are observed. An analogous effect of eddies on the frequency spectra of SST is discussed in Frankignoul (1981) and Hall and Manabe (1997).

The -4 slope spiciness signal is isolated after filtering out the high-wavenumber variability associated with the eddy field, consistent with the section 2 anomalous advection model, which applies to long-wavelength variability only. Verification of the -4 signal in observations thus requires a long-term, large-spatial-scale record of temperature and salinity.

7. Surface versus interior processes

Spiciness variability in the thermocline is affected by surface processes that form anomalies at isopycnal outcrops and subsequent forcing in the interior that alters spiciness along advective pathways. Outcrop anomalies influence interior spiciness via the mean advection term on the lhs of Eq. (2), which has been neglected here because S_{10} is dominated by interior anomalous advection forcing (Fig. 5). Outcrop anomalies in the model are forced by realistic surface heat fluxes (Nonaka and Sasaki 2007; Bindoff and McDougall 1994), anomalous Ekman advection (Mignot and Frankignoul 2003), and small-scale eddy variability. However, surface freshwater fluxes contain only seasonal variability. The combination of too-shallow mixed layers (see section 3) and limited vertical resolution precludes faithful representation of the $O(10$ m) diapycnal mixing that can inject spiciness anomalies into the base of the mixed layer (Yeager and Large 2004; Luo et al. 2005; Johnson 2006; Yeager and Large 2007) in regions of unstable vertical salinity gradients and weak density stratification (Fig. 6).

A gauge of the missing surface processes' importance is a comparison of the model spiciness variance to observations at HOT, which is located downstream of the model domain. Although the signals are not correlated,

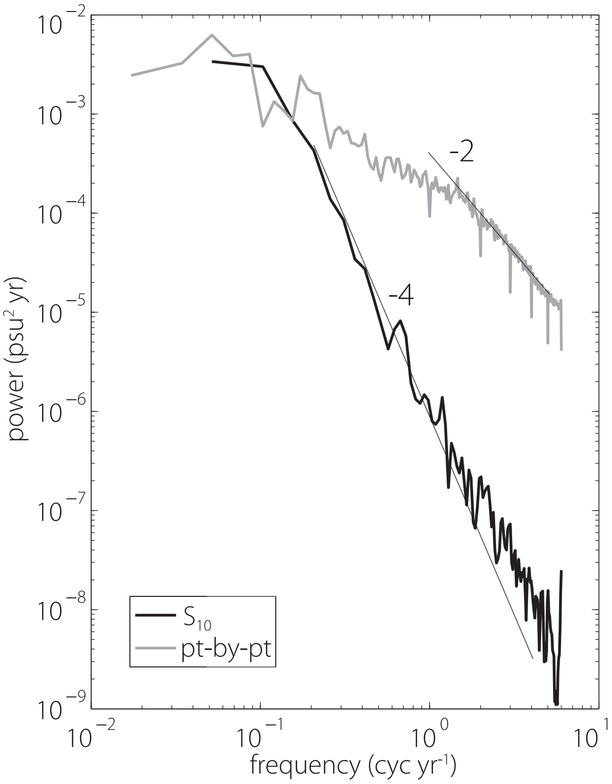

FIG. 10. Frequency spectrum of S_{10}, the spatially averaged isopycnal salinity (black); compare to the isopycnal salinity spectrum computed separately at each point in mask and subsequently averaged over all points in mask (gray; psu^2 yr). The thin black lines show -4 and -2 slopes for reference.

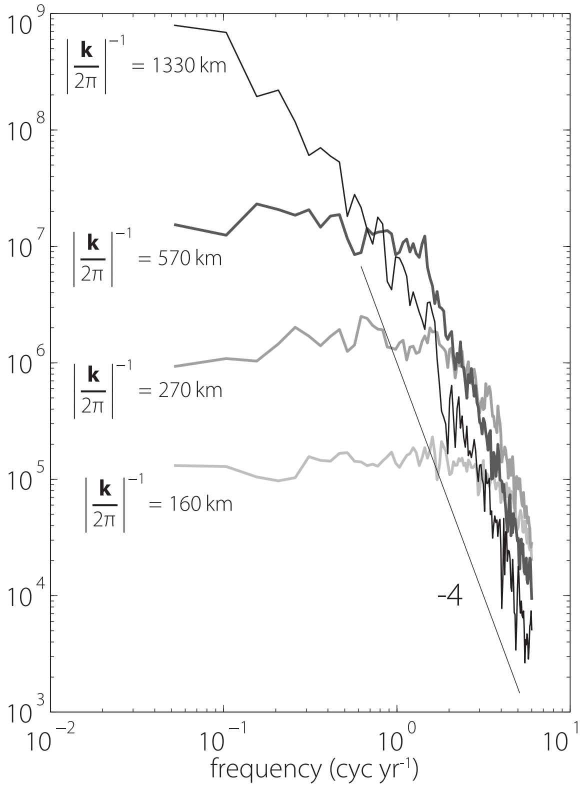

FIG. 11. Wavenumber–frequency spectrum of salinity (psu^2 yr m) on the $\sigma_\theta = 26$ kg m^{-3} isopycnal for varying bands of horizontal wavenumber $|\mathbf{k}|$. The thin black line shows a -4 slope for reference.

the S_{10} standard deviation is 0.03 psu, compared to 0.04 psu on the same isopycnal ($\sigma_\theta = 26$ kg m^{-3}) at HOT (Fig. 1 in Lukas and Santiago-Mandujano 2008); since the HOT signal is measured at one location, spatially averaging would likely reduce the variance somewhat, as shown in section 6. The similar order of magnitude of S_{10} and the HOT signal suggests that interior anomalous geostrophic advection, rather than surface processes, could be the dominant forcing of low-frequency spiciness variability at HOT.

Prior studies have attempted to link the HOT observations to surface freshwater fluxes only (Lukas 2001; Lukas and Santiago-Mandujano 2008). Although Lukas and Santiago-Mandujano (2008) did mention that wind stress curl variations are capable of affecting salinity by altering circulation patterns, a subsequent adjoint sensitivity analysis (Stammer et al. 2008) did not include wind stress curl as a possible forcing mechanism. Thus, it is left for future study to quantify the relative importance of freshwater flux variability and Ekman pumping–forced anomalous advection, though observations elsewhere in the Pacific support the anomalous advection hypothesis: Kessler (1999) found that subsurface salinity anomalies at 165°E during 1984–97 were consistent with changes in zonal advection and the wrong sign to be explained by subducting surface anomalies, whereas Suga et al. (2000) was unable to link subsurface salinity anomalies at 137°E to upstream freshwater fluxes and stated that "in situ processes such as anomalous advection or mixing can be just as important as changes of the thermohaline forcing at the outcrop regions, in forcing anomalies in the temperature and salinity along isopycnal and level surfaces."

8. Summary and discussion

The generation of low-frequency variability of a passive tracer is investigated using the example of density-compensated temperature and salinity anomalies, or spiciness. In contrast to prior studies that linked subsurface spiciness variability directly to surface thermohaline forcing (Lukas 2001; Lukas and Santiago-Mandujano 2008; Nonaka and Sasaki 2007; Laurian et al. 2009), this study focuses on the generation of spiciness variability in the thermocline by anomalous geostrophic currents acting against mean spiciness gradients, or anomalous geostrophic advection. A coupled Markov model [Eqs. (12) and (13)] is developed in which stochastic wind stress curl forces the large-scale first baroclinic mode pressure, which in turn forces the anomalous geostrophic advection of spiciness. The Markov model predicts that this "double integration" of atmospheric forcing results in a frequency spectrum of large-scale spiciness that has a 0 slope for low frequencies and a -4 slope for high frequencies, separated by a smooth transition around the damping coefficients μ and λ (Fig. 1). An eddy-permitting regional model hindcast of the northeast Pacific (1950–2007) confirms that time series of large-scale spiciness variability are exceptionally smooth, with frequency spectra $\propto \omega^{-4}$ for frequencies greater than 0.2 cpy.

The double integration that is fundamental to anomalous advection acts as an efficient low-pass filter and thus has consequences for decadal climate. Low-frequency variability in spiciness and other dynamically passive tracers can be efficiently generated in the thermocline by off-equatorial, stochastic Ekman pumping; nearly all variance in this study occurs at frequencies below 0.2 cpy. Spiciness variability can advect to the tropics and affect equatorial climate (Schneider 2004); this one-way forcing mechanism provides a null hypothesis for explaining equatorial climate anomalies. Anomalous advection also provides a null hypothesis for attributing decadal variability in biogeochemical tracers like oxygen (Ito and Deutsch 2010).

At shorter spatial scales (wavelengths less than ~500 km), the spiciness frequency spectrum is whitened by mesoscale eddies. The spiciness frequency spectrum at one grid point, which integrates variance over all wavenumbers, shows a slope closer to -2 than -4 (Fig. 10). Only after applying a spatial average or low-wavenumber bandpass filter does the -4 slope signal emerge. The eddies can be averaged over, indicating they are not spatially coherent at the larger scale of the spiciness signal. The implication is that a large spatial array of measurements, such as Argo, is necessary to observe the variance of spiciness or any other passive tracer subject to anomalous advection in the thermocline.

This study has focused on the generation of spiciness variance in the thermocline, but anomalous geostrophic advection also influences surface spiciness (Mignot and Frankignoul 2003). However, other processes directly forced by the atmosphere are important at the surface, such as anomalous freshwater fluxes (Lukas 2001), heat fluxes (Nonaka and Sasaki 2007), and Ekman advection. The "fast" atmospheric forcings leave a signature -2 slope in the frequency spectrum of spiciness at the surface, where isopycnals outcrop; it is only in the thermocline where anomalous geostrophic advection becomes dominant, leaving its signature -4 slope. The frequency spectrum of interior spiciness therefore discerns whether variability is of surface or interior origin.

The damping coefficients $\mu = 0.5\ \mathrm{yr}^{-1}$ and $\lambda = 0.6\ \mathrm{yr}^{-1}$ (radian frequency) were estimated from the frequency spectra of S_{10} and η_{10}, respectively, and correspond to decadal time scales. The negative feedback processes that μ and λ correspond to have not been explored here. Only in the simplified physics of section 2 are μ and λ constant, because Rossby waves cause λ to vary with distance from the eastern boundary (Frankignoul et al. 1997), whereas the curving trajectory of the mean flow, outcrop patterns, and mean advection (Frankignoul and Reynolds 1983) affect the spatial distribution of μ. Dottori and Clarke (2009) showed the importance of Rossby waves for low-frequency variability off California but did not consider their effect on temperature and salinity spectra. It is thus left for future study to consider how the interplay between Rossby waves and anomalous advection causes spiciness spectra to vary in space.

Acknowledgments. This study benefited from discussions with Drs. Bo Qiu, Peter Müller, and Glenn Carter. The authors gratefully acknowledge the comments of two anonymous reviewers that helped improve an earlier version of the manuscript. This research was supported by the National Science Foundation through Grant OCE-0550233. The International Pacific Research Center is sponsored by the Japan Agency for Marine–Earth Science and Technology (JAMSTEC), by NASA through Grant NNX07AG53G, and by NOAA through Grant NA17RJ1230.

REFERENCES

Bindoff, N. L., and T. J. McDougall, 1994: Diagnosing climate change and ocean ventilation using hydrographic data. *J. Phys. Oceanogr.,* **24,** 1137–1152.

Bograd, S. J., and R. J. Lynn, 2003: Long-term variability in the Southern California Current System. *Deep-Sea Res. II,* **50,** 2355–2370.

Chelton, D. B., P. A. Bernal, and J. A. McGowan, 1982: Large-scale interannual physical and biological interaction in the California Current. *J. Mar. Res.,* **40,** 1095–1125.

Chhak, K. C., E. Di Lorenzo, P. Cummins, and N. Schneider, 2009: Forcing of low-frequency ocean variability in the northeast Pacific. *J. Climate,* **22,** 1255–1276.

Combes, V., and E. Di Lorenzo, 2007: Intrinsic and forced interannual variability of the Gulf of Alaska mesoscale circulation. *Prog. Oceanogr.,* **75,** 266–286.

Cummins, P. F., and G. S. E. Lagerloef, 2002: Low-frequency pycnocline depth variability at Ocean Weather Station P in the northeast Pacific. *J. Phys. Oceanogr.,* **32,** 3207–3215.

——, and ——, 2004: Wind-driven interannual variability over the northeast Pacific Ocean. *Deep-Sea Res. I,* **51,** 2105–2121.

Davis, R. E., 1976: Predictability of sea surface temperature and sea level pressure anomalies over the North Pacific Ocean. *J. Phys. Oceanogr.,* **6,** 249–266.

de Boyer Montégut, C., G. Madec, A. S. Fischer, A. Lazar, and D. Iudicone, 2004: Mixed layer depth over the global ocean: An examination of profile data and a profile-based climatology. *J. Geophys. Res.,* **109,** C12003, doi:10.1029/2004JC002378.

Di Lorenzo, E., and Coauthors, 2008: North Pacific Gyre Oscillation links ocean climate and ecosystem change. *Geophys. Res. Lett.,* **35,** L08607, doi:10.1029/2007GL032838.

——, and Coauthors, 2009: Nutrient and salinity decadal variations in the central and eastern North Pacific. *Geophys. Res. Lett.,* **36,** L14601, doi:10.1029/2009GL038261.

Dottori, M., and A. J. Clarke, 2009: Rossby waves and the interannual and interdecadal variability of temperature and salinity off California. *J. Phys. Oceanogr.,* **39,** 2543–2561.

Frankignoul, C., 1981: Low-frequency temperature fluctuations off Bermuda. *J. Geophys. Res.,* **86** (C7), 6522–6528.

——, and K. Hasselmann, 1977: Stochastic climate models, Part II. Application to sea-surface temperature anomalies and thermocline variability. *Tellus,* **29,** 289–305.

——, and R. W. Reynolds, 1983: Testing a dynamical model for mid-latitude sea surface temperature anomalies. *J. Phys. Oceanogr.,* **13,** 1131–1145.

——, P. Müller, and E. Zorita, 1997: A simple model of the decadal response of the ocean to stochastic wind forcing. *J. Phys. Oceanogr.,* **27,** 1533–1546.

Fukumori, I., T. Lee, B. Cheng, and D. Menemenlis, 2004: The origin, pathway, and destination of Niño-3 water estimated by a simulated passive tracer and its adjoint. *J. Phys. Oceanogr.,* **34,** 582–604.

Gu, D., and S. G. H. Philander, 1997: Interdecadal climate fluctuations that depend on exchanges between the tropics and extratropics. *Science,* **275,** 805–807.

Hall, A., and S. Manabe, 1997: Can local linear stochastic theory explain sea surface temperature and salinity variability? *Climate Dyn.,* **13,** 167–180.

Hasselmann, K., 1976: Stochastic climate models. Part 1, Theory. *Tellus,* **28,** 473–485.

Iselin, C. O. D., 1939: The influence of vertical and lateral turbulence on the characteristics of the waters at mid-depths. *Trans. Amer. Geophys. Union,* **20,** 414–417.

Ito, T., and C. Deutsch, 2010: A conceptual model for the temporal spectrum of oceanic oxygen variability. *Geophys. Res. Lett.,* L03601, doi:10.1029/2009GL041595.

James, I. N., and P. M. James, 1989: Ultra-low-frequency variability in a simple atmospheric circulation model. *Nature,* **342,** 53–55.

Johnson, G. C., 2006: Generation and initial evolution of a mode water θ–S anomaly. *J. Phys. Oceanogr.,* **36,** 739–751.

Kalnay, E., and Coauthors, 1996: The NCEP–NCAR 40-Year Reanalysis Project. *Bull. Amer. Meteor. Soc.,* **77,** 437–471.

Kessler, W. S., 1999: Interannual variability of the subsurface high salinity tongue south of the equator at 165°E. *J. Phys. Oceanogr.,* **29,** 2038–2049.

Lagerloef, G. S. E., 1995: Interdecadal variations in the Alaska gyre. *J. Phys. Oceanogr.,* **25,** 2242–2258.

Large, W. G., J. C. McWilliams, and S. C. Doney, 1994: Oceanic vertical mixing: A review and a model with a nonlocal boundary layer parameterization. *Rev. Geophys.,* **32,** 363–403.

Laurian, A., A. Lazar, G. Reverdin, K. Rodgers, and P. Terray, 2006: Poleward propagation of spiciness anomalies in the North Atlantic Ocean. *Geophys. Res. Lett.,* **33,** L13603, doi:10.1029/2006GL026155.

——, ——, and ——, 2009: Generation mechanism of spiciness anomalies: An OGCM analysis in the North Atlantic subtropical gyre. *J. Phys. Oceanogr.,* **39,** 1003–1018.

Ledwell, J. R., A. J. Watson, and C. S. Law, 1993: Evidence for slow mixing across the pycnocline from an open-ocean tracer-release experiment. *Nature,* **364,** 701–703.

Levitus, S., R. Burgett, and T. P. Boyer, 1994: *Salinity*. Vol. 3, *World Ocean Atlas 1994,* NOAA Atlas NESDIS 3, 99 pp.

Liu, Z., and S.-I. Shin, 1999: On thermocline ventilation of active and passive tracers. *Geophys. Res. Lett.,* **26,** 357–360.

Lukas, R., 2001: Freshening of the upper thermocline in the North Pacific subtropical gyre associated with decadal changes in rainfall. *Geophys. Res. Lett.,* **28,** 3485–3488.

——, and F. Santiago-Mandujano, 2008: Interannual to interdecadal salinity variations observed near Hawaii: Local and remote forcing by surface freshwater fluxes. *Oceanography,* **21,** 46–55.

Luo, Y., L. M. Rothstein, R.-H. Zhang, and A. J. Busalacchi, 2005: On the connection between South Pacific subtropical spiciness anomalies and decadal equatorial variability in an ocean general circulation model. *J. Geophys. Res.,* **110,** C10002, doi:10.1029/2004JC002655.

Mantua, N. J., S. R. Hare, Y. Zhang, J. M. Wallace, and R. C. Francis, 1997: A Pacific interdecadal climate oscillation with impacts on salmon production. *Bull. Amer. Meteor. Soc.,* **78,** 1069–1079.

Marchesiello, P., J. C. McWilliams, and A. Shchepetkin, 2001: Open boundary conditions for long-term integration of regional oceanic models. *Ocean Modell.,* **3,** 1–20.

——, ——, and ——, 2003: Equilibrium structure and dynamics of the California Current System. *J. Phys. Oceanogr.,* **33,** 753–783.

Masumoto, Y., and Coauthors, 2004: A fifty-year eddy-resolving simulation of the World Ocean—Preliminary outcomes of OFES (OGCM for the Earth Simulator). *J. Earth Simulator,* **1,** 35–56.

Mignot, J., and C. Frankignoul, 2003: On the interannual variability of surface salinity in the Atlantic. *Climate Dyn.,* **20,** 555–565.

Müller, P., and J. Willebrand, 1986: Compressibility effects in the thermohaline circulation: A manifestation of the temperature–salinity mode. *Deep-Sea Res.,* **33,** 559–571.

Munk, W., 1981: Internal waves and small-scale processes. *Evolution of Physical Oceanography,* B. A. Warren and C. Wunsch, Eds., The MIT Press, 264–291.

Nonaka, M., and H. Sasaki, 2007: Formation mechanism for isopycnal temperature–salinity anomalies propagating from the eastern South Pacific to the equatorial region. *J. Climate,* **20,** 1305–1315.

Qiu, B., 2003: Kuroshio Extension variability and forcing of the Pacific decadal oscillations: Responses and potential feedback. *J. Phys. Oceanogr.,* **33,** 2465–2482.

Ren, L., and S. C. Riser, 2010: Observations of decadal time scale salinity changes in the subtropical thermocline of the North Pacific Ocean. *Deep-Sea Res. II,* **57,** 1161–1170.

Roemmich, D., and J. McGowan, 1995: Climatic warming and the decline of zooplankton in the California Current. *Science,* **267,** 1324–1326.

Sasaki, Y. N., N. Schneider, N. Maximenko, and K. Lebedev, 2010: Observational evidence for propagation of decadal spiciness anomalies in the North Pacific. *Geophys. Res. Lett.,* **37,** L07708, doi:10.1029/2010GL042716.

Schneider, N., 1999: Pacific thermocline bridge revisited. *Geophys. Res. Lett.,* **26,** 1329–1332.

——, 2000: A decadal spiciness mode in the tropics. *Geophys. Res. Lett.,* **27,** 257–260.

——, 2004: The response of tropical climate to the equatorial emergence of spiciness anomalies. *J. Climate,* **17,** 1083–1095.

——, and B. D. Cornuelle, 2005: The forcing of the Pacific decadal oscillation. *J. Climate,* **18,** 4355–4373.

——, E. Di Lorenzo, and P. P. Niiler, 2005: Salinity variations in the southern California Current. *J. Phys. Oceanogr.,* **35,** 1421–1436.

Schwing, F. B., and R. Mendelssohn, 1997: Increased coastal upwelling in the California Current System. *J. Geophys. Res.,* **102** (C2), 3421–3438.

Shchepetkin, A., and J. C. McWilliams, 2005: The Regional Oceanic Modeling System (ROMS): A split-explicit, free-surface, topography-following-coordinate ocean model. *Ocean Modell.,* **9,** 347–404.

Smith, T. M., and R. W. Reynolds, 2004: Improved extended reconstruction of SST (1854–1997). *J. Climate,* **17,** 2466–2477.

Spall, M. A., 1993: Variability of sea surface salinity in stochastically forced systems. *Climate Dyn.,* **8,** 151–160.

Stammer, D., S. Park, A. Kohl, R. Lukas, and F. Santiago-Mandujano, 2008: Causes for large-scale hydrographic changes at the Hawaii Ocean time series station. *J. Phys. Oceanogr.,* **38,** 1931–1948.

Suga, T., A. Kato, and K. Hanawa, 2000: North Pacific Tropical Water: Its climatology and temporal changes associated with the climate regime shift in the 1970s. *Prog. Oceanogr.,* **47,** 223–256.

Tailleux, R., A. Lazar, and C. J. C. Reason, 2005: Physics and dynamics of density-compensated temperature and salinity anomalies. Part I: Theory. *J. Phys. Oceanogr.,* **35,** 849–864.

Vallis, G. K., 2006: *Atmospheric and Oceanic Fluid Dynamics*. Cambridge University Press, 745 pp.

Veronis, G., 1972: On properties of seawater defined by temperature, salinity, and pressure. *J. Mar. Res.,* **30,** 227–255.

Williams, P. D., E. Guilyardi, R. Sutton, J. Gregory, and G. Madec, 2007: A new feedback on climate change from the hydrological cycle. *Geophys. Res. Lett.,* **34,** L08706, doi:10.1029/2007GL029275.

Yeager, S. G., and W. G. Large, 2004: Late-winter generation of spiciness on subducted isopycnals. *J. Phys. Oceanogr.,* **34,** 1528–1547.

——, and ——, 2007: Observational evidence of winter spice injection. *J. Phys. Oceanogr.,* **37,** 2895–2919.